Available online at www.sciencedirect.com

ScienceDirect

Journal of Magnesium and Alloys 9 (2021) 1521–1536

www.elsevier.com/locate/jma

The role of Ca, Al and Zn on room temperature ductility and grain boundary cohesion of magnesium

Supriya Nandy, Shao-Pu Tsai, Leigh Stephenson, Dierk Raabe, Stefan Zaefferer*

Max-Planck Institut für Eisenforschung, Düsseldorf 40237, Germany

Received 16 July 2020; received in revised form 10 February 2021; accepted 4 March 2021
Available online 28 May 2021

Abstract

It is know from literature that small additions (<1 wt%) of Ca, Al and Zn significantly improve the intrinsic ductility of Mg. The exact role of each element, both qualitatively and quantitatively, and their combined effects, however, are poorly understood. Here we achieved a much clearer view on the quantitative role of each element with respect to ductility improvement and on the collaborative effect, particularly of Ca and Zn in Mg. Some of our findings and conclusions are in disagreement with data and interpretation found in literature. Four different alloys, namely, Mg-0.1 Ca, Mg-0.1 Ca-1 Al, Mg-0.05 Ca-1 Al, Mg-0.1 Ca-2 Al-1 Zn (all are in wt%) were selected for this investigation. All alloys were treated such that approx. similar grain sizes and textures were obtained. This largely excludes the effect of extrinsic factors on ductility. EBSD-guided slip trace analyses reveal that the addition of Ca eases activation of prismatic and pyramidal II slip systems. Using in-situ deformation experiments in SEM and atom probe tomography observations of grain boundaries direct evidence is given for the individual and synergetic effects of Ca and Zn on grain boundary cohesion as an important contribution to improve the ductility of these alloys. We conclude that Ca reduces the slip anisotropy and ameliorates ductility, however, the weak grain boundary cohesion in the Mg-0.1 wt% Ca alloy limits the material's tensile ductility. The addition of Zn alters the Ca segregation at the grain boundaries and helps to retain their cohesive strength, an effect which thus enables higher ductility and strength. The further addition of Al primarily improves the strength. The results show that the balanced influence of reduced slip anisotropy on the one hand and increased grain boundary cohesion on the other hand allow to design a high strength high ductility rare-earth free Mg alloy.

Keywords: Magnesium–Calcium–Zinc alloys; Ductility; Slip system determination; grain boundary cohesion.

1. Introduction

With up to twice the specific strength of mild and/or low carbon steels, magnesium and its alloys possess great potential for mobile structural components. In contrast to its good specific strength the hexagonal close packed magnesium suffers from low room-temperature ductility caused by the limited availability of deformation systems at ambient temperature. Basal and prismatic dislocation glide, being major deformation systems, do not provide the five necessary independent modes of straining according to the Taylor-von Mises criterion. Since the past few decades, researchers attempted different thermomechanical processing routes to improve the room temperature formability of Mg and its alloys mainly by extrinsic factors, namely grain refinement and texture weakening. On the other hand, alloying, for example with rare-earth elements, decreases the intrinsic room-temperature brittleness by easing higher-order deformation systems such as pyramidal $<c+a>$ glide, as well as contraction twinning and double twinning. Activation and mobility of $\langle c+a\rangle$ slip in Mg alloys are of long-standing research interest. Sandlöbes et al. [1,2] claimed that the addition of rare-earth elements to Mg decreases the I_1 stacking fault energy. According to the literature, I_1 stacking faults are presumably a heterogeneous source for $\langle c+a\rangle$ dislocation nucleation [3]. Other researchers [4,5] also claimed that early immobilisation of $\langle c+a\rangle$ dislocations leads to anomalous temperature dependence of tensile strength

* Corresponding author.
E-mail address: s.zaefferer@mpie.de (S. Zaefferer).

https://doi.org/10.1016/j.jma.2021.03.005

in Mg alloys and to reduced room temperature ductility. Recently, using MD simulations, Wu and Curtin [6] showed a fast decomposition of a glissile $\langle c+a \rangle$ dislocation core to different sessile partials. Following this work, Wu et al. [7] also proposed two counteractive processes of $\langle c+a \rangle$ slip, namely, (a) decomposition and immobilisation and (b) cross-slip and multiplication. These authors suggested an alloy design criterion based on the energy barrier difference between process (a) and (b) and showed that addition of Y to Mg leads to more cross-slip and multiplication of $\langle c+a \rangle$ slip than in the case of pure Mg. Their calculations also showed that Ca should have a similar but less pronounced effect as RE elements, while Zn should have the opposite effect. Earlier, Yoo et al. [8] also suggested that the difference in free energy of dissociation of $\langle c+a \rangle$ dislocations on {10–11} and {11–22} planes, respectively, plays an important role in mobilization of $\langle c+a \rangle$ dislocations. Tang and El-Awady [9] indicated that the mobility of $\langle c+a \rangle$ dislocations on {10–11} planes is easier than on {11–22} planes because the former planes possess less lattice resistance. The above compilation of knowledge in this field shows that the increased activity of $\langle c+a \rangle$ dislocations in ductile Mg alloys is considered in literature mainly a question of mobility of these dislocations and not of their nucleation.

Efforts have been made to explore alloying additions which may show similar behaviour as the rare earth elements. Chino et al. [10] found that the addition of Ca improves room temperature ductility and stretch formability of Mg–Zn alloys while its addition does not affect the ductility of Mg–Al alloys. These researchers found that addition of Ca to Mg and Mg–Zn reduced the basal texture intensity and improved the room temperature formability. They concluded that the texture change was responsible for the increased ductility, but the facts could also be interpreted inversely, i.e. that the increased ductility, caused by more balanced slip system activation would result in a weaker texture. Using theory-guided alloy prototyping, Sandlöbes et al. [11] recently demonstrated that a Mg–Al–Ca alloy exhibits excellent room temperature ductility when Ca is added up to the room temperature solubility limit of 0.1 wt.%. These authors correlated the improvement in ductility with activation of $\langle c+a \rangle$ slip via a change of I_1 stacking fault energy. Surprisingly, the addition of Ca beyond its room temperature solubility limit in Mg weakens the texture but also drastically reduces the room temperature formability. Zeng et al. [12] investigated the effect of minute additions of Ca and Zn to Mg. These authors concluded, however without direct evidence of grain boundary chemistry, that Zn addition may improve the grain boundary cohesion and therefore ameliorate the room temperature ductility in Mg–Zn–Ca alloys. Nevertheless, no quantitative evidence, neither for the intrinsic ductilization by a change of slip system activity, nor for the change of grain boundary strength by small additions of Ca and the role of Zn and Al in Mg, has been given so far.

The present study aims to fill this gap. Besides pure Mg, four alloys with different Ca, Al and Zn contents were selected. All alloys contained Ca. One binary Mg–Ca alloy and two ternary Mg–Al–Ca alloys with different Ca content were investigated to understand the effect of Ca in balancing the slip systems and the solution strengthening efficacy of Al. Finally, one alloy contained Ca, Al and Zn was selected to realize the effect of Zn on grain boundary strength and improved mechanical properties. For this alloy particularly high strength and ductility was expected based on previous work. All alloys were hot rolled and annealed such that approximately similar grain sizes and comparable textures were obtained. Static tensile tests were then carried out at room temperature to measure the ductility. The deformation behaviour was then further analysed using electron back-scatter diffraction (EBSD)-assisted slip trace analyses. Note, that slip trace analysis considers the joint effect of nucleation and mobility of dislocations. Next, the critical resolved shear stress ratios for different slip systems were estimated using the frequency of trace appearance for all of the investigated alloys. Grain boundary chemistry for selected alloys was determined using atom probe tomography and further correlated with grain boundary de-cohesion. The extended room temperature plasticity of Mg–Al–Zn–Ca alloy and role of Zn, Ca and Al is discussed in terms of estimated CRSS-ratio values and grain boundary strength.

Table 1
Chemical composition of the four investigated alloys.

Alloy	Al	Ca	Zn	Mg
X01		0.1		Balance
AX101	1	0.1		Balance
AX100	1	0.05		Balance
AZX2101	2	0.1	1	Balance

2. Materials and methods

Four rare-earth free Mg-alloy melts were prepared in an induction furnace and cast at 1023 K in a Cu mould. The alloy chemistry was measured using glow discharge emission spectrometry and the composition of the cast alloys is shown, together with the acronyms used in the following text, in Table 1. According to equilibrium calculations at 723 K using Factsage 7.3, Mg-0.1 wt% Ca (X01) and Mg-1 wt% Al-0.05 wt% Ca (AX100) alloys consist of only single phase hcp Mg while Mg-1 wt% Al-0.1 wt% Ca (AX101) and Mg-2 wt% Al-1 wt.% Zn-0.1 wt% Ca (AZX2101) contain <0.1% Al_2Ca Laves phase in addition to hcp-Mg, respectively. The cast billets with a thickness of 29 mm were hot-rolled at 703 K (soaking time of 15 min) using a 10% reduction per pass to a total reduction of > 90%, corresponding to 2 mm sheet thickness. Intermediate short (up to 3 min) annealing after each pass was performed to maintain the temperature of rolling. Subsequently the samples were annealed at 723 K for 15 min followed by water quenching to obtain a fully recrystallized microstructure. Flat dog-bone-type tensile samples were fabricated from the rolled and annealed sheets using electrical discharge machining (EDM). These were grinded up to 4000-grit SiC paper before the tests. Uniaxial tensile tests of all selected

alloys were carried out along 0°, 45° and 90° to the rolling direction at ambient temperature. The tensile tests were performed using a Kammrath & Weiss tensile stage at an initial strain rate of 5×10^{-4} s^{-1}. Minimum four tests were performed at each condition. The global strain during the tensile tests was estimated by digital image correlation (DIC) using the Aramis system (GOM GmbH).

The microstructure of the annealed specimens was investigated using EBSD with 15 kV primary beam incident on 70° tilted specimens. Free standing specimens were metallographically prepared up to 4000 grit SiC paper and then polished using 1 μm diamond suspension. Next, electro-chemical polishing was carried out to remove residual surface deformation from grinding. A mixture of ethanol and phosphoric acid (5:3 by volume) was used as electrolyte with a stainless steel plate as cathode. A potential difference of 2 V was applied for 2 h at 298 K. Finally, precision argon ion polishing was performed using GATAN PECS with 2.1 keV and 32 μA for up to 4 h. One polished tensile sample for each alloy was deformed up to 5% to allow slip line observation using SEM. Quasi in-situ EBSD-guided slip trace analyses were performed empolying a Zeiss 1540 XB SEM operated at 10 kV using secondary electrons.

SEM in-situ tensile tests were carried out to estimate grain boundary cracking with progressive loading for X01 and AZX2101 alloys. An in-house designed-in-situ tensile stage was used and mounted in a Zeiss 1540 XB SEM. The geometry of the in-situ tensile samples is presented in supplementary information (Fig. S1). Tensile tests were carried out at 298 K at a nominal strain rate of 5×10^{-4} s^{-1}. Every 30 s the tests were stopped and microstructural investigations were carried out. Several images were taken using secondary electron imaging at each stop.

Grain boundary chemistry was measured using atom probe tomography (APT). Specimens from X01 and AZX2101 alloys were prepared using a cross-beam SEM (FIB) instrument (30 kV SEM-FIB FEI Helios PFIB Dual Beam) for the atom probe study. The specimens were sharpened by FIB milling at 30 kV followed by a final cleaning step at 5 kV/12 pA current. Finally, the tip radii were measured to be 20-80 nm. APT was done using voltage pulsing mode at 50 K with a pulse fraction and rate of 0.15 and 200 kHz respectively using a LEAP 5000XS. The mass-spectra were analysed using the commercially available software package IVAS 3.8.4. The chemistry of two different random high angle grain boundaries was measured for each selected alloys. Before performing APT investigations the tips were observed by transmission Kikuchi pattern mapping to verify the existence of grain boundaries inside of the relevant volume. In all tips random high angle grain boundaries were determined.

3. Results

3.1. Microstructure and mechanical properties

The microstructure images in Fig. 1 display the fully recrystallized equiaxed microstructure of all investigated alloys after annealing. The average grain sizes of X01, AX101, AX100 and AZX2101 alloys are, respectively, 29 (±11), 19 (±8), 28 (±14) and 24 (±10) μm. Additionally, Fig. 1 also depicts the (0002) pole figures and their maximum intensities for the respective alloys. The (0002) pole figure is assumed to be sufficiently characteristic of the texture of the alloys. It shows a strongly preferred alignment of the (0002) poles with the normal direction (ND) of the sheet and a slight splitting of the (0002)‖ND peak about the rolling direction (RD), as it is typical for most rolled and recrystallized Mg alloys [13,14]. In Table 2 we report, together with the grain size, the maximum pole density in multiples of random distribution (mrd), the pole splitting width about RD in degree and the full width at half maximum (FWHM) of the pole density distribution. We estimate the FWHM using a Gaussian fit of (0001) pole distribution along RD. The textures of the different alloys are relatively similar but a few characteristics should be pointed out: the alloy X01 shows the lowest maximum pole density and the widest pole distribution while AZX2101 shows the highest density and narrowest distribution. The pole splitting is largest for AX101 and smallest for AZX2101.

Fig. 2 depicts the room temperature tensile stress–strain responses in rolling direction (RD), under 45° to RD and in transverse direction (TD). Furthermore, the strain hardening curves $\frac{d\sigma}{d\varepsilon}(\varepsilon)$ are displayed in the supplementary material (Fig. S2). The obtained results are summarized in Table 3. The alloy X01 demonstrates about a 3-fold increase in uniform elongation (UE) compared to pure Mg. AX100 alloy, with the smallest Ca content, exhibits the lowest ductility amongst all investigated alloys. Interestingly, AZX2101 possesses the highest ductility as well as the highest strength amongst all the investigated materials. The strain hardening exponents are estimated using the true stress-strain curves and are also presented in Table 3. Generally, the values for the exponent (n) range between 0.2 and 0.3 for all investigated alloys. The images in Fig. 3 represent the fracture surfaces of the tensile specimens tested along RD for all investigated alloys. Fig. 3(a) and 3(c) shows the fracture surfaces of X01 and AX100 alloy. These alloys depict mostly featureless flat terraces and tear ridges. Further, AX101 alloy exhibits few dimples on the fracture surface (Fig. 3(b)). Finally, the fracture surface of AZX2101 alloy mostly shows dimples indicating typical ductile failure.

3.2. Slip trace analyses and critical resolve shear stress ratio estimation

5% tensile deformed samples were selected to determine the deformation behaviour of all investigated alloys. The intersection of dislocations on well defined slip planes with the free specimen surfaces introduces slip steps on the polished specimen surface. These slip traces were measured. Additionally the orientations of the corresponding grains were determined using EBSD. Fig. 4 depicts a typical workflow for graphical slip trace analyses. Using the MTEX toolbox, we calculated stereographic projections of the different slip planes for the investigated grains. The following slip systems

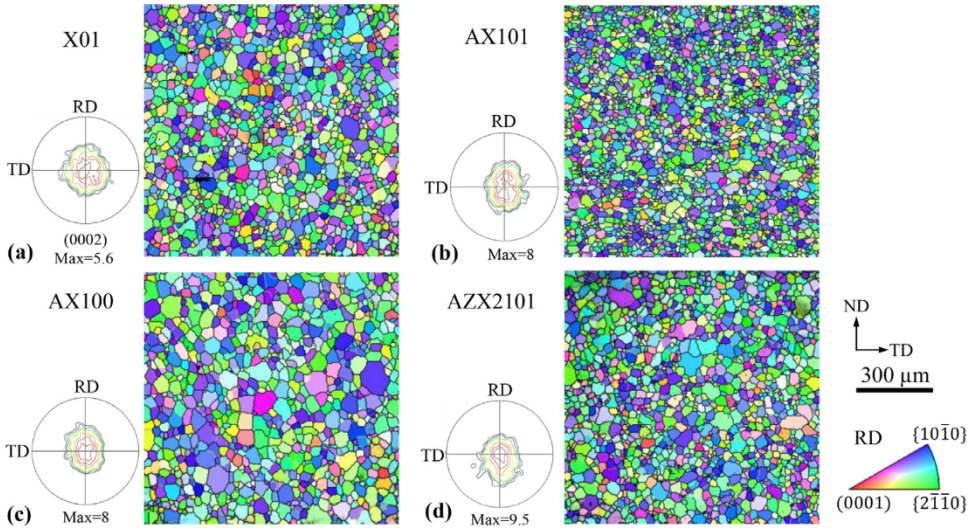

Fig. 1. Texture and microstructure of the investigated alloys obtained by EBSD mapping. The alloy acronyms are described in Table 1. Textures are displayed as (0002) pole figures calculated by spherical harmonics series up to a rank of 32 without sample symmetry. Microstructures are displayed by inverse pole figure maps of the rolling direction. Large angle grain boundaries (>15°) are indicated by black lines, low angle boundaries (2°−15°) by yellow ones.

Table 2
Characteristic values for texture information and grain size for different alloys.

Alloy	(0001) pole intensity (mrd)	RD split (°)	Full width at half maxima along RD (°)	Grain size (μm)
X01	5.6	5	30	29
AX101	8	7.5	24	19
AX100	8	0	22	28
AZX2101	9.5	0	20	24

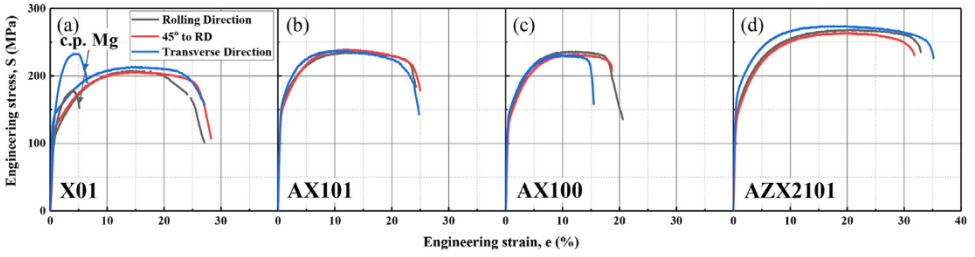

Fig. 2. Engineering stress strain curves for different alloys; (a) X01, (b) AX101, (c) AX100 and (d) AZX2101 in rolling direction (black), 45° to the rolling direction (red) and in transverse direction (blue). Figure (a) additionally contains the reference data from pure magnesium (in black).

Table. 3
Summary of tensile properties for all investigated alloys. YS=Yield strength, UTS=Ultimate tensile strength, UE=Uniform elongation, TE= Total elongation and *n*= strain hardening exponent.

Alloys	Loading	YS(MPa)	UTS(MPa)	UE (%)	TE(%)	n
Pure	RD	70±5	173±1	4.6 ± 0.2	5.5 ± 0.2	0.4 ± 0.03
Mg	TD	120±10	220±10	5 ± 0.1	7 ± 0.2	0.4 ± 0.01
X01	RD	96±2.5	180±9	13±0.2	25±0.5	0.28±0.01
	45°	119±4.8	213±5.2	15±0.14	25±0.7	0.29±0.004
	TD	137±4.3	214±3	14±0.3	25±1.6	0.25±0.01
AX101	RD	147±9.5	248±12	16±0.8	27±2.3	0.24±0.01
	45°	120±4.5	232±5	11.8 ± 0.1	25±0.7	0.27±0.01
	TD	157±3.2	247±4.6	10±0.1	20±0.5	0.24±0.01
AX100	RD	111±2.7	208±6	13±0.3	22±0.6	0.31±0.002
	45°	124±2.2	226±2.1	12±0.2	20±1.7	0.28±0.002
	TD	143±2	226±2.3	10±0.2	19±1	0.25±0.002
AZX2101	RD	131±4	265±2.3	21±0.2	34±0.3	0.27±0.005
	45°	120±6	251±9.6	20±0.2	31±0.4	0.30±0.004
	TD	165	274±1.4	18±0.1	32±0.8	0.23±0.003

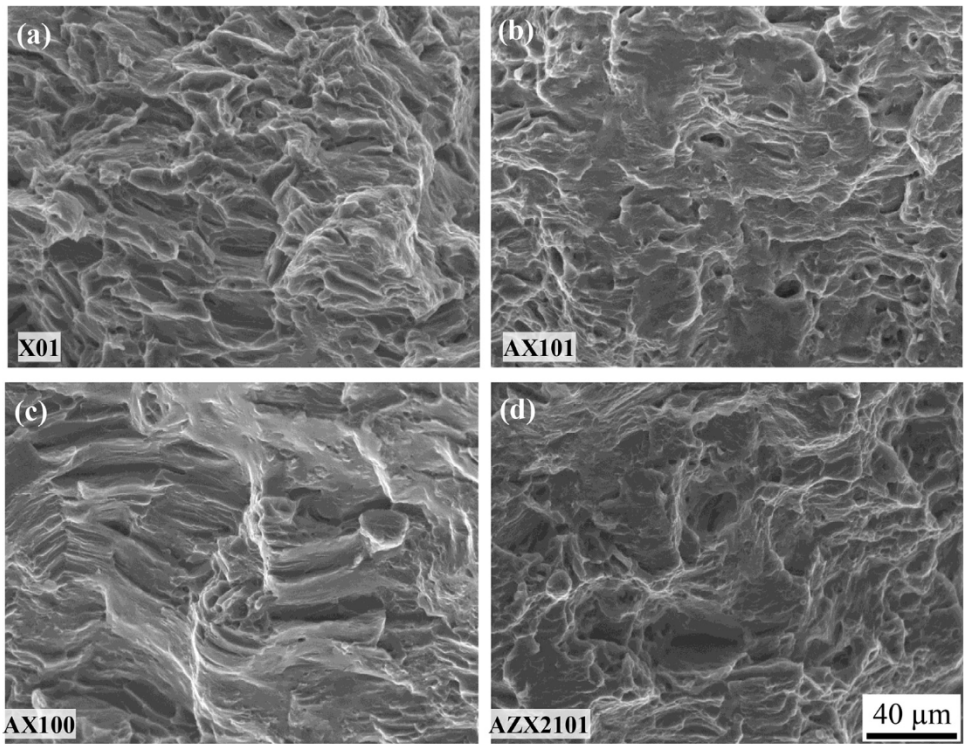

Fig. 3. Typical fracture surfaces after tensile failure for all investigated alloys; (a) X01, (b) AX101, (c) AX100 and (d) AZX2101 alloy.

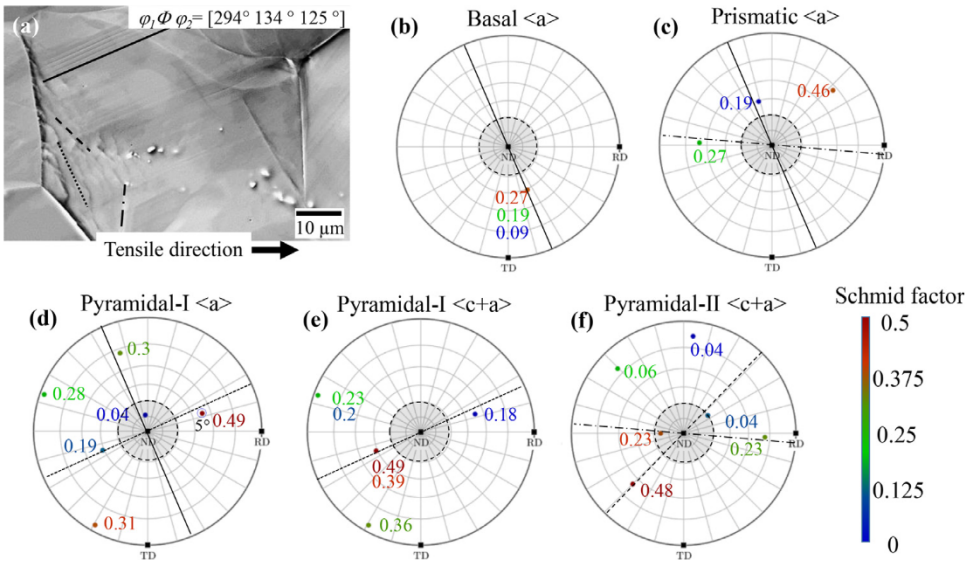

Fig. 4. Principle of slip trace analysis for critical resolved shear stress ratio determination. (a) Slip lines are highlighted using straight black lines of different style; tensile direction and Euler angles are displayed. (b)-(f) Stereographic projections of different slip systems for the grain displayed in (a). The numbers and symbol colours indicate the Schmid factors for the particular slip system. The black straight lines drawn in the stereographic projection are the potential slip plane loci for the respective slip traces. They are obtained by a 90° rotation of the slip traces observed in (a) drawn through the centre of the respective projections. The shaded areas in the centre indicate the range where slip trace analysis is highly inaccurate.

were evaluated: basal ⟨a⟩ (B), prismatic ⟨a⟩ (P_0), pyramidal I ⟨a⟩ ($P_{I<a>}$), pyramidal I ⟨$c+a$⟩ ($P_{I<c+a>}$) and pyramidal II ⟨$c+a$⟩ (P_{II}). The poles in the different projections are furthermore marked in colours according to the magnitude of the Schmid factors (S-factor) for the respective slip systems. Subsequently, lines perpendicular to the trace lines are drawn through the centre of the pole figure. These lines must intersect the pole of the correct slip system. Unfortunately, the slip system evaluation is not unique in some cases since several slip systems may have identical or very close traces. In the case in Fig. 4, for example, the solid line traces could be B, as well as P_0 or $P_{I<a>}$. The line-dotted trace could be P_0 but

Table 4
A typical example of observed slip traces identifications using workflow in Fig. 5 for single grain in X01 alloy.

Schmid factor	0–0.05	0.05–0.1	0.1–0.15	0.15–0.2	0.2–0.25	0.25–0.3	0.3–0.35	0.35–0.4	0.4–0.45	0.45–0.5
Activated deformation system	–	–	–	–	Basal	–	–	Extension twin	–	P-I $\langle c+a\rangle$ P-II $<c+a>$

also P_{II} and the dotted trace would fit to $P_{I<a>}$ and $P_{I<c+a>}$. In order to resolve this ambiguity we assume that, if a slip system is activated at all, then, under the condition that the grain can deform freely (Sachs-condition), it will always first activate that variant with the highest S-factor. This is also in line with the Bishop-Hill theory of polycrystal deformation where the first activated slip systems are always those with the highest S-factors and the ones that ensure mutual grain-to-grain strain compatibility are those that are activated due to back stresses. Thus in Fig. 4 the correct slip system would be most likely that, which intersects a pole in red colour. With this assumption we find for the present example that the solid line corresponds to B slip, and the dashed trace to P_{II}. Only the dotted trace would still be ambiguous, being either $P_{I<a>}$ or $P_{I<c+a>}$. For this case the decision is finally made in favour of $P_{I<c+a>}$, based on the proximity of the trace to the slip system pole. (see also the error discussion further below). These analyses were repeated in a microstructural patch consisting of more than 100 grains for every alloy.

The appearance of observed slip traces (might be more than one for a particular slip system) are then counted and classified according to their respective S-factors. For instance, Table 4 describes the counting results from the above-mentioned case for the X01 alloy. The graph in Fig. 5(a) exemplarily describes for alloy X01 the number of observed slip traces and extension twins within the investigated grains, binned using Schmid factor binning windows of 0.05. We report all measured trace analysis data for all alloys in Table S1 in the supplementary material section. These statistically relevant materials datasets have been used to determine the corresponding critical resolve shear stress ratios (CRSS-ratio) among the different deformation systems of all investigated materials as described by Li et al. [15] for an hcp-Ti alloy. These authors first assumed unit CRSS-ratios and then determine all potential slip systems by calculating the number of possible symmetrically equivalent variants for all slip systems irrespective of their respective S-factors. Next they considered a cubic fitting function to weigh the possible deformation modes with respect to the magnitude of the S-factor. Using the number of weighted possible deformation systems, the authors generated a probability density function. Multiplication of the probability density function with the total number of observations then yielded the expected number of active deformation systems assuming a CRSS ratio equal to 1. Next, the CRSS-ratios were varied to minimize the difference between the expected number of active deformation systems and the observed number of slip system. A similar methodology has been adapted for the present study to compare the CRSS ratios between the different investigated Mg alloys. Instead of a cubic weight function of the S-factor values, we applied a linear function in order to avoid overfitting of higher S-factor data and under fitting of lower S-factor data. However, following the previous studies we also tested different weight factors and observed no significant change in CRSS ratios. The graphs in Fig. 5 indicate the process flow (for X01 as an example) to calculate the CRSS-ratios. Fig. 5(a) displays, as mentioned above, the observation counts of different slip systems for different S-factors. Fig. 5(b) displays the counts of all slip systems that would be hypothetically observed in the investigated grains (with their experimentally observed orientations) if the CRSS of all slip systems would be identical (e.g. equal to 1) and the S-factor would not play a role. Fig. 5(c) displays the hypothetical data of Fig. 5(b) but multiplied with a linear function of the S-factor to take into account the different resolved shear stresses acting on the different slip systems. Finally, these data need to be adapted to the data in Fig. 5(a) by modifying the CRSS ratios of the different slip systems. This is done as follows: Let P_{ij}^0 be the expected number of slip traces for the ith S-factor- binning window and jth deformation mode (assuming CRSS-ratios=1) (from Fig. 5(c)) and N_{ij} is the observed number of slip traces (from Fig. 5(a)). $P_{ij}^0 \neq N_{ij}$ as CRSSs are assumed identical (compare between Fig. 5(a) and 5(c)). If one considers that the CRSSs are not identical then P_{ij}^0 becomes $P_{ij} = \frac{c}{\tau_j} P_{ij}^0$. τ_j is the CRSS of the jth deformation system. Following Li et al. [15], an error equation is formulated as follows:

$$d\left(\tau_b \tau_{P_0} \tau_{P_{I\langle a\rangle}} \tau_{P_{I\langle c+a\rangle}} \tau_{P_{II}} \tau_{TT}\right) = \sqrt{\sum_{i,j} \left(P_{ij} - N_{ij}\right)^2} = \sqrt{\sum_{i,j} \left(\frac{1}{\tau_j} P_{ij}^0 - N_{ij}\right)^2} \quad (1)$$

As we take $c = 1$ and $\tau_b = 1$, τ_j represent the CRSS-ratios for other deformation systems. We consider 10 binning windows for S-factors (i = 1,2,3,…,10) and account for the appearance of 6 different deformation systems (j = 1,2,3,…,6). Error minimization of Eq. (1) yields the optimum CRSS-ratios for the selected alloy after 5% deformation under room temperature tension. Fig. 6 reports the obtained CRSS-ratios for all investigated alloys. Fig. 5(d), finally, compares the distribution of the observed deformation system activation to the one re-calculated using optimised CRSS-ratio for X01 alloy. The differences between these two plots are reasonably small. This validates the comparison of the CRSS-ratios between different alloys. Note that the absolute values of CRSSs are not in the scope of the present paper. Instead, we highlight the comparative differences in CRSS ratios in Fig 6. A first look

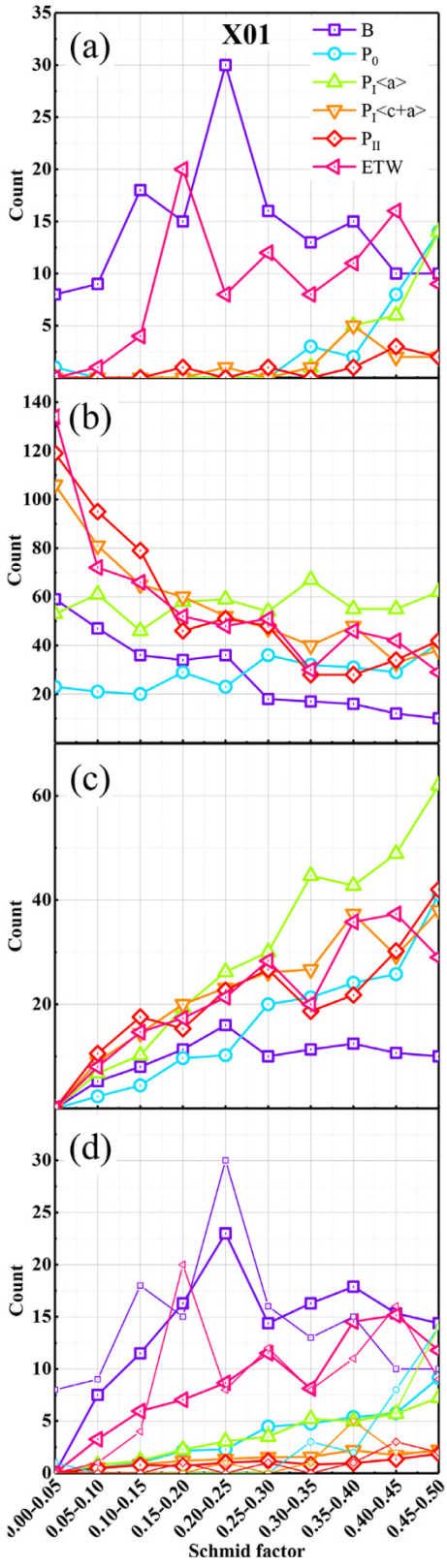

Fig. 5. Demonstration of typical process flow for calculation of CRSS ratios for the X01 alloy. (a) Number of experimentally observed deformation systems, (b) number of available deformation systems in the microstructure, (c) Schmid factor-corrected available deformation systems and (d) comparison between experimentally observed and re-calculated numbers using optimized CRSS ratios for different deformation systems.

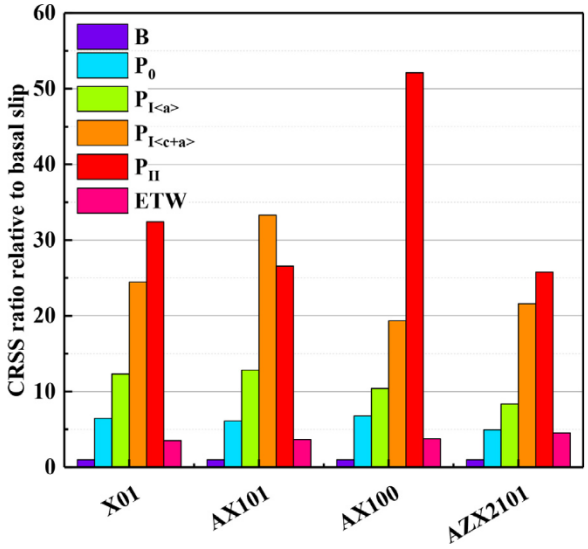

Fig. 6. Estimated CRSS-ratios of different slip and twin systems for all investigated alloys. CRSS of basal slip is set to 1 as reference.

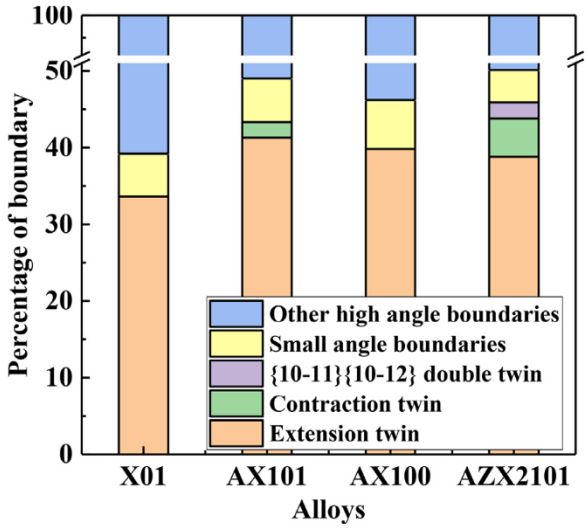

Fig. 7. Estimated boundary fractions for all investigated alloy after 5% tensile deformation.

on this graph reveals that the alloy AX100 (with 0.05 wt-% Ca) shows the highest variation for the CRSSs of the different slip systems while AZX2101 shows the lowest. The two other alloys which both contain 0.1 wt-% Ca are about equal. A decreasing variation of the slip system's CRSSs indicates that the activation of different slip systems is more balanced. When analysing these data in more detail it appears that in the AX100 alloy (which contains the smallest amount of Ca of all the alloys) the higher-order slip systems e.g. pyramidal-II $\langle c+a \rangle$ are calculated to be twice as hard as those in all other investigated alloys. This indicates that the addition of Ca to Mg alloys reduces the CRSS-ratios of higher-order deformation systems.

Fig. 7 displays the twin boundary fractions measured using EBSD after 5% of tensile deformation. The $\{10\bar{1}2\}\langle 10\bar{1}1\rangle$ extension twin fraction is largest and almost similar in all

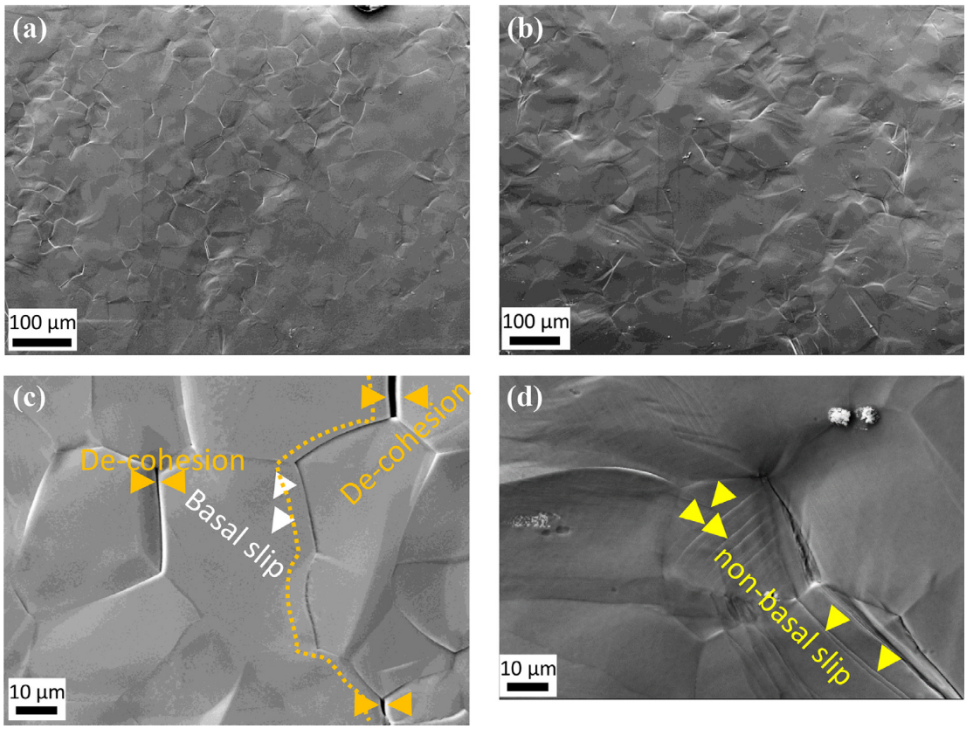

Fig. 8. Demonstration of grain boundary de-cohesion in two selected alloys: (a) and (c) X01 alloy; (b), and (d) AZX2101 alloy. (a) and (b) at low magnification; (c) and (d) high magnification. X01 shows a significantly higher amount of de-cohesion.

selected alloys. Extension twins accommodate some deformation along the ⟨c⟩ axis but the amount of shear is rather limited. This indicates that increased ductility in the selected alloys is primarily due to activation of non-basal slip. Further, $\{10\bar{1}1\}\langle 10\bar{1}2\rangle$ contraction twins are also present in both AX101 and AZX2101 alloys whereas, $\{10\bar{1}1\}-\{10\bar{1}2\}$ double twins are only present in the latter one.

3.3. Grain boundary characterization

In order to investigate the influence of Ca and Zn on the grain boundary strength, SEM in-situ tensile deformation experiments of polished specimens of X01 and AZX2101 alloys were performed while observing the deformation microstructure evolution using secondary electrons. A typical example for this experiment is shown in Fig. 8, showing the microstructures of alloys X01 (a and c) and AZX2101 (b and d) after 5% deformation. Severe grain boundary cracking is observed in the X01 alloy, while the alloy AZX2101 mainly remains undamaged. The three-dimensional nature of the cracked grain boundary was revealed and examined by using focused Ga-ion milling at 30 kV and 1 nA. A typical FIB-cut of a grain boundary for the X01 alloy is presented in Fig. 9(a). In this case, the crack continues to more than 10 µm below the surface. Grain boundary cracking was further quantified based on the microscopic appearance of the cracks. We used ImageJ v1.46r to characterize and analyse the grain boundary cracking based on boundary contrast. The image contrast was enhanced such that the cracked boundaries could be thresholded against other microstructural features. Using the edge finding algorithm, we characterized the edge segments of these boundaries and manually checked the appearance of any over/underestimation of grain boundaries. Feret size analysis was then used to estimate the cracked grain boundary length. The total grain boundary length was determined using the EBSD maps obtained before deformation. Fig. 9(a) displays the percentage of cracked grain boundaries for the two investigated alloys X01 and AZX2101. It shows that the addition of Zn in the AZX2101 alloy significantly reduces grain boundary cracking to almost one third of the non-Zn containing alloy. Assuming that the crack *length* fraction is equal to the *area* fraction of the cracked grain boundaries and cracking occurs perpendicularly to the global stress axis, it is possible to calculate a corrected true stress taking into account the decreased cross-section in alloys X01 and AZX2101. The results are presented in Fig. 9b. It is noteworthy that the corrected true stress values of both alloys are nearly the same. This observation suggests that the weak grain boundaries reduce the hardening capacity of X01 to nearly 50%. To better understand the role of Ca and Zn, the grain boundary chemistry was investigated using atom probe tomography (APT). Fig. 10 displays one atom map for each of the two alloys, X01 and AZX2101. The segregation of Ca is displayed using 2 at.% Ca isosurfaces. Typical composition profile across the highlighted interfaces using a cylindrical region of interest (marked as a transparent golden cylinder) are displayed as well. A black arrow exhibits the direction along the composition profiles. In the Ca-atom map of Fig 10(a) two ROI named as C-1 and C-2 are considered. C-1 delineates the composition of the Ca- rich clusters whereas, C-

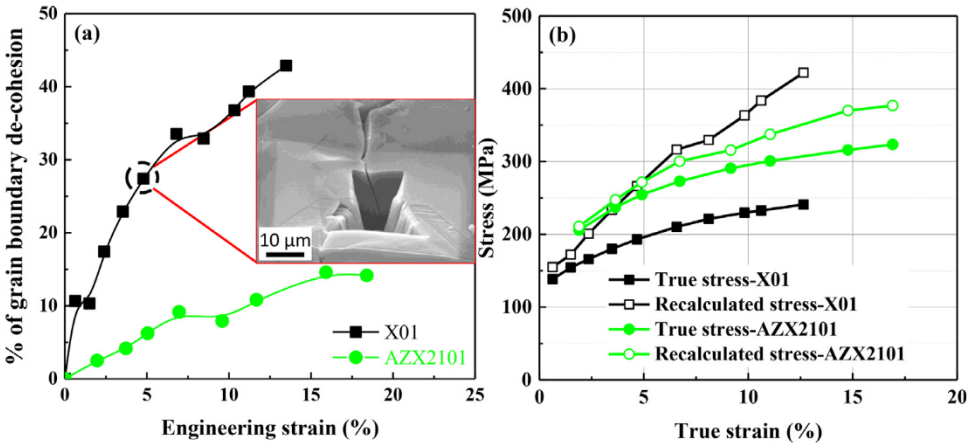

Fig. 9. (a) Quantitative estimation of the fraction of fractured grain boundaries with progressive deformation for selected alloys. The fraction is calculated from surface observations in Fig. 8, assuming the surface line length fraction to be equal to volume surface area fraction. The inset shows the 3D nature of a fractured grain boundary after 5% deformation in X01 alloy. (b) Recalculated true stress taking into account the reduction of cross section area by cracking of grain boundaries for X01 and AZX2101 alloys.

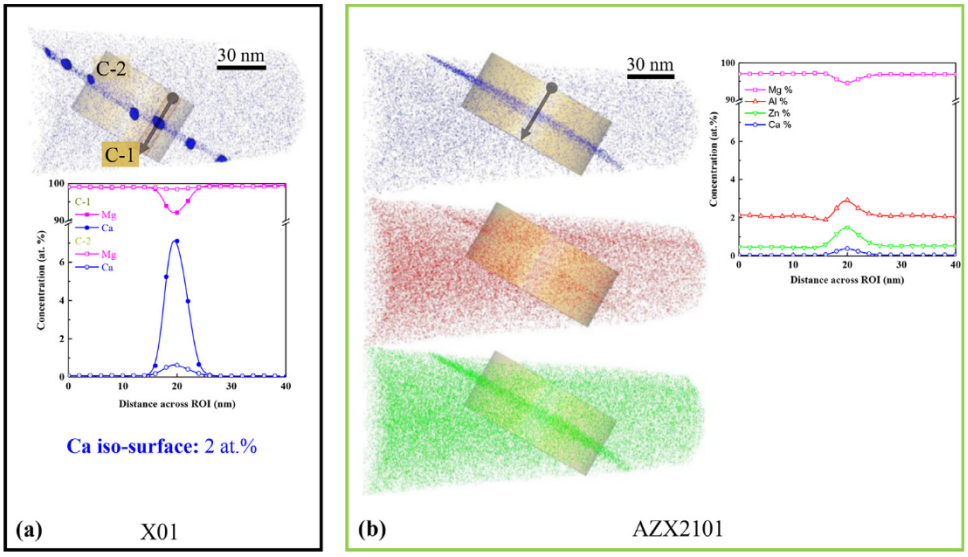

Fig. 10. Atom probe tomography of random high angle grain boundaries of (a) X01 and (b) AZX2101 alloys. 2 at.-% Ca isosurfaces are shown as blue interfaces and the respective concentration profiles from two regions of interest (blue cylinder) are represented in the corresponding inset. In the profile in (a) the solid symbols indicate the profile along C1, the open symbols those measured in C2 along the same direction.

2 describes an average composition profile across the grain boundary. The profiles show that the nature of segregation is different between two investigated alloys. In the X01 alloy, Ca enrichment takes place in form of nearly spherical clusters of ~6–10 nm diameter with bulk Ca concentration exceeding 7 at.%. At the core of these clusters in the X01 alloy the composition of Ca is even higher (up to 15 at%, see supplementary Fig. S3). We believe that these spherical clusters of Ca to be precursors of the Mg_2Ca Laves phase. In contrast, Ca segregates homogenously to the boundary in the AZX2101 alloy and the amount is nearly an order of magnitude smaller compared to that in the X01 alloy. Interestingly, the average composition profile for Ca across the grain boundary is similar in both alloys. For X01 the Ca segregates up to 0.62 at.% while for AZX2101 the value is nearly 0.4 at.%. These values are about 10 times larger than the bulk Ca concentration in both alloys. Furthermore, in the alloy AZX2101 co-segregation of Zn and Al with Ca as indicated in Fig 10(b) is observed. The Al and Zn contents are found to be increased by a factor of 1.5 and 3 times, respectively compared to their bulk concentrations.

4. Discussion

4.1. Slip system error consideration

Whether the slip system assignment made in section 3.2 is correct depends on the accuracy of the EBSD measurements and on the validity of the Sachs – Bishop-Hill assumptions about the local boundary conditions. The accuracy of the

measurement can be readily estimated from the accuracy of the basal slip planes. As basal slip is the most easily activated system it forms very sharp and well-visible slip traces as observable in Fig. 5(a). We find that in most cases the basal poles are just about 1° to 2° away from the measured slip traces, which is approximately the accuracy we expect from the EBSD measurements. The observed trace position depends furthermore on the local planarity of the observed surface. This planarity has no influence if the observed slip trace stands exactly perpendicular to the surface and it has the strongest influence when it is near-parallel to it. The traces are, thus, the more precise, the more perpendicular the planes are to the sample surface, i.e. the further away is a plane pole from the centre of the pole figure. As shown by Wang and Zaefferer [16] - if we assume that the specimen surface is maximum 2° away from being perpendicular to the electron beam - the error in trace determination may be as big as 15° but already for planes standing 30° to the surface the error is below 2° The 30°-boundary above which the trace analysis is very reliable is indicated in the example provided in Fig. 4 by a gray shading around the centre of the pole figures.

In contrast to basal slip, the traces of other slip systems are usually not as well defined, probably because they are less prominently activated or/and because the dislocations on them tend to undergo more frequent cross slip. This appears reasonable from observing Fig. 4(a), where the non-basal slip planes are rather wavy. Thus, the accuracy for these systems is estimated to be rather in the order of 5° than 2° for basal slip. Despite the waviness of the slip lines there are sufficiently long, rather straight sections along these slip traces to be quite sure that the determined slip planes are not a result of frequent cross slip but occur due to slip on well defined planes.

A second crucial assumption underneath the slip system analysis is the validity of the Sachs or respectively Bishop-Hill boundary conditions, meaning that the microscopic, local stress tensor can be approximated by the macroscopic assuming grain-to-grain strain compatibility. This implies that the local slip system selection can be derived from the macroscopic tensile stresses and the local crystal orientation. In the present case we consider only small strains ($< 5\%$). This means that strain accomodation in different grains may not yet be very important. Furthermore, only grains at the free surface are observed and flat samples are tested under tensile stresses. Also, the Bishop-Hill theory, which translates the Taylor theory for polycrystal deformation from strain space into stress space, states that it is always those slip systems with the highest Schmid factors that are actived first in a grain; strain compatibility is fulfilled – through back-stresses – through the activity of secondary slip.

Strain compatibility is not achieved homogeneously across grains, but deformation proceeds heterogeneously, first at grain boundaries and triple junctions. In order to check how heterogeneous the stresses are distributed in the material we performed local stress measurements using cross correlation EBSD (CC EBSD) [17]. This technique allows, with the lateral resolution of EBSD ($\sim$ 500 nm for Mg [18]), to determine the strain and stress tensor distribution across individual grains at the surface of a sample. Fig. 11 displays the von Mises stress distributions that were measured in microstructure sections of the materials X01 and AZX2101 tensile deformed to 2% of strain. These maps show that the stresses at the grain boundaries are usually higher than those in the grain interiors and that this distinction is more severe for the sample X01 than for the sample AZX2101. In order to obtain more quantitative data the von Mises stress values were integrated along pixels close the grain boundaries and across pixels in the grain interior. The integrated values show that for sample in X01 alloy, the grain boundary stresses are about twice larger than the grain boundary interior values, while only marginal grain boundary stresses are built up in sample AZX2101. This shows that the Sachs assumptions that we use here to approximate the local stresses are reasonably fulfilled for sample AZX2101. For this sample the CRSS data displayed in Fig. 6 appear very reliable. In contrast, for the sample X01 (and probably for also for the other samples not containing Zn) the CRSS anisotropy is probably underestimated: since most of the non-basal slip systems are found close to the grain boundaries and as the CC-EBSD data show that there are twice higher stresses at these locations, the CRSS values for non-basal slip systems may be higher than those displayed in Fig. 6.

The local and global crystallographic texture plays an important role also for the activation of different slip systems in general. The trace analyses and estimation of the CRSS ratios are, therefore, expected to be biased by the sharp near basal texture of the present samples. Nevertheless, as the investigated materials exhibit comparably similar textures the reported CRSS ratios appear similarly comparable, though they don't allow an absolute assessment of the CRSS ratios. An assessment of the effect of texture on activation of slip systems maybe done by comparing the average S-factors obtained for the different basal slip systems. Average basal S-factor for X01 alloy is 0.26 and same for other alloys are 0.21. These values are reasonable close to be sure that the CRSS ratio values from different materials can be compared to each other.

In conclusion we assume that the analysis performed here appears reasonably accurate to allow correct slip system determination. It appears that the CRSS values for the alloy AZX2101 are the most realistic ones. For the other alloys the CRSS values of non-basal slip may be underestimated by maximum a factor 2. Taking this into account a proper comparison of the different activities of the underlying deformation systems is possible for all investigated alloys.

4.2. Comparability of microstructures and textures

The annealing textures and grain sizes are relatively similar for all alloys investigated. Nevertheless, a short assessment of the influence of grain size and texture for the obtained yield strength shall be made here. The grain size influences the yield strength by the Hall-Petch relation, $\sigma = \sigma_0 + k\, d^{-\frac{1}{2}}$. Grain size of AX101 alloy is 34% finer compared to X01 alloy; this will lead to only 17% increase in yield strength in AX101 alloy compared to X01. Considering the Considère

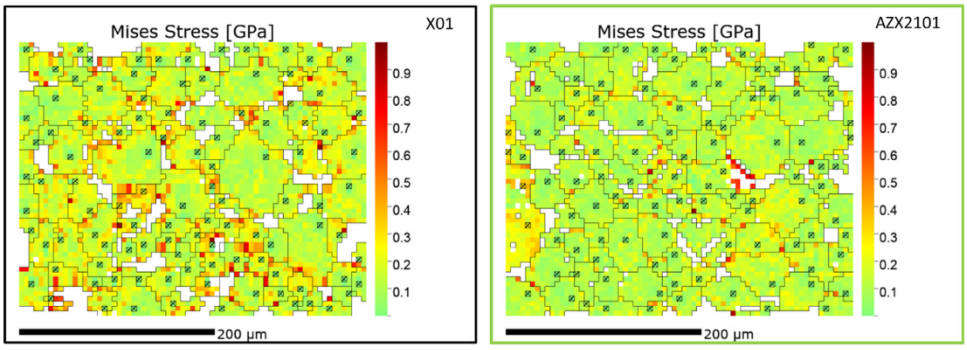

Fig. 11. Von-Mises stress distribution inside of every grain, measured relative to the crossed pixel marked in every grain using cross-correlation EBSD analysis of (a) X01 and (b) AZX2101 alloys. Grain boundaries usually show the highest relative stress values. In X01 grain boundary stresses are significantly higher than those in AZX2101.

criterion and assuming same hardening behaviour, we calculated that 17% increase in the yield strength would decrease the uniform elongation of the alloy by 2%. These calculations show that 34% finer grain size has insignificant contribution towards strength and ductility. In terms of texture, as mentioned in the previous section, the average basal slip S-factors for all alloys are comparable which indicates that there is no significant influence of texture on mechanical properties. Nevertheless, the observed anisotropy in elongation and strength for some of the alloys may be attributed to the slight split of the basal pole intensities towards RD. Nevertheless, the variation of mechanical properties stays for all cases below 10%. Note that the textures are a result of hot rolling and recrystallization and will, therefore, not be discussed further since this paper focusses on room-temperature ductility. The above discussion indicates that the variation in mechanical properties are mostly due to intrinsic effects related to the specific alloying additions.

4.3. Comparison of mechanical data documented in literature

From literature it is well-known, and confirmed here by our results compiled in Fig. 3 and Table 3, that Ca dramatically increases the ductility of pure Mg (0.1 wt-% Ca increases UE by a factor 3) and also of the Al-containing alloys AX100 and AX101 (an increase of the Ca content from 0.05 to 0.1 wt-% increases UE by 20%). Al addition, in contrast, does not affect the tensile elongation considerably but mainly increases the strength of the X01 alloy by 40% in AX101 alloy. Zn seems to increases both, ductility and strength by 60%.

Although these trends are well-documented in literature a quantitative assessment of the correlative effects of Ca, Al and Zn is missing and even trends are difficult to extract when comparing different results from literature. To obtain a clearer view we compiled all suitable data (20 data sets altogether) available from the literature [10–12,19–22] in addition to our own current results. Only such data were selected, which are comparable to our data in terms of texture, grain size and deformation conditions. Fig. 12 displays (a) the uniform elongation and (b) the ultimate tensile strength values collected for different Mg–Al–Zn–Ca alloys over the ternary composition of these alloys (the data is also provided as supplementary Table S2). The axes represent the concentrations in wt-% of the three different alloying elements, Ca, Al and Zn. The colour of every data point displays its corresponding value. Our own values are marked by additional red dashed circles around the data points in Fig. 12.

There is large scatter in the data but some general trends can be extracted:

(i) With respect to the addition of Ca it is found that an addition of 0.1% Ca is significantly improving the ductility while higher amounts deteriorate it; on the other hand, the Ca content does not significantly affect the ultimate tensile strength (UTS) values.
(ii) Aluminium seems to improve both, ductility and strength but our own data show that it affects strength more than ductility.
(iii) Samples without Zn generally have poor ductility. The addition of Zn always improves both strength and ductility.

Points (i) and (ii) will be dealt with here below, point (iii) will be discussed in more detail in section 4.3.

Point (ii) is a rather diffuse observation. According to the present results and the available literature data, Al primarily acts as a solute solution strengthening element. In contrast, Zn additions alone apparently are not effective in improving the strength of binary Mg–Zn alloys. The combination of Al and Zn additions reduce the slip anisotropy by selectively strengthening basal slip as suggested by Kim et al. [22] and Shi et al. [23]. Consequently, prismatic and/or pyramidal slip systems become easier activated compared to basal slip.

With respect to the effect of Ca additions, point (i) mentions that ductility improves up to 0.1 wt% but deteriorates for higher amounts. This effect may be explained by the finding that alloying more than 0.1 wt% Ca apparently leads to formation of the C14 (Mg_2Ca) phase at grain boundaries which then decreases ductility [11]. Our atom probe tomography data, in fact, indicate as well that the sample which contains only Ca-additions forms clusters at the grain boundaries, which may

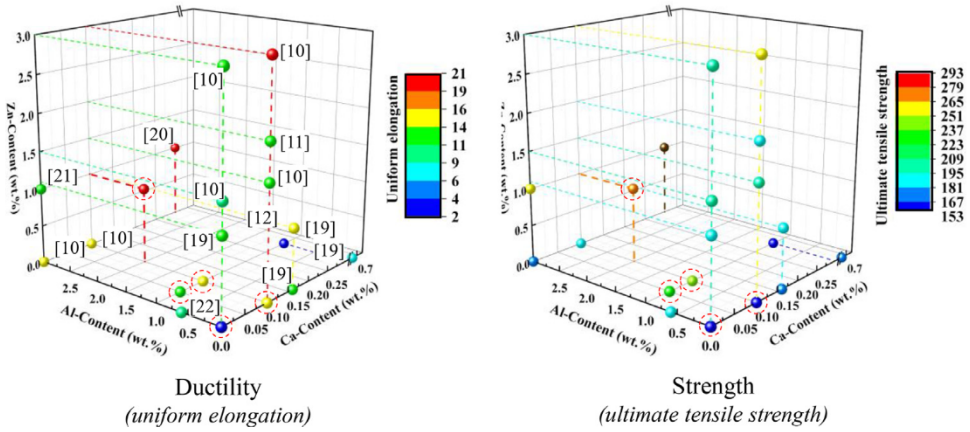

Fig. 12. Display of (a) uniform elongation and (b) ultimate tensile strength as function of Ca, Al and Zn content for different AZX alloys including data from literature and own data. Data encircled in red are from the present study.

be regarded as precursors for Laves phase formation. The atom probe data will be discussed in detail in section 4.5.

The effect of Ca additions was investigated in great detail by Chino et al. [24] who argued that the reduction of the charge density due to addition of Ca in Mg introduces solution softening. They also showed that addition of Ca facilitates formation of double kinks in Mg alloys and thus increases the glissle properties of dislocation motion. In other words, the addition of Ca increases the mobility of the dislocations through lowering the kink formation barriers. Therefore, explaining point (i) requires a detailed look into the here performed slip system analysis. It appears that the addition of Ca and Zn to Mg improves the ductility of ternary and the quaternary Mg–Al–Zn–Ca alloys dramatically, i.e. by 4 times relative to pure Mg. This data survey indicates a conjugate role of Ca and Zn in Mg alloys to improve the room temperature ductility as well as the strength. In order to understand the roles of Ca and Zn for deformation of Mg alloys, we consider in the next section the critical resolved shear stress ratio for different alloys based on 5% tensile-deformed samples.

4.4. Slip system activation

Our present work yields quantitative data on the critical resolved shear stress ratios of different slip systems in different alloys. These data are largely absent in literature but the few which exist [25,26, 35–38,27–34] shall be discussed in the following in conjunction with those we found. For pure Mg at 0 K [25], for example, reported CRSS ratio values in the order of 1: 22: 394 for the basal, prismatic, and pyramidal II slip, respectively using MD simulation. Very early single crystal experimental data by Obara et al. [28] reported a ratio of 1: ~100 (P_{II}). In contrast, recent experimental investigations by micro-pillar compression yielded values of 1: ~2.2 (P_{II}): 1 (ext. twinning). With respect to alloys, Chapuis and Liu [30], for example, reported values for AZ31 of 1: 18 (P_0): 22 (P_{II}): 6 (ext. twinning) based on fitting of data of crystal plasticity modelling to real deformation. Also Jain and Agnew [31] determined relative CRSS values for AZ31 based on modelling and found 1: 3.2: 5: 1.5. Most recently, Wu et al. reported values of 1: 3 (P_I) for an alloy with 4 at-% Y. Nayyeri et al. [35] reported values of 1: 13 (P_I) obtained by nanoindentation for a Zn–Nd-containing alloy. Akhtar and Teghtsoonian [37] and Stanford and Barnett [39] discussed that addition of Zn up to 1 wt% significantly reduces relative CRSS between prismatic to basal slip at room temperature. Our own results, which are the most comprehensive of all documented data, show that also Ca additions decrease the CRSS ratios for higher-order deformation systems. For the X01 and AX101 alloys with 0.1% Ca we find crss-ratios in the order of 1: 7: ~28. For the alloy AX100 containing only 0.05% Ca we find 1: 7: 53. Finally, for the quarternary alloy containing Al, Zn and Ca AZX2101 we find 1: 5: 36 (P_{II}). Note here that according to the strain compatibility discussion in section 5.4.2, the estimated CRSS-ratio in the X01 alloy and possibly also in the AX100 and AX101 alloys are underestimated by a factor of two.

The above mentioned data and further data found in literature are compiled in Table 5. In this table shading colours are used to mark particular groups of results: yellow marks those data which are obtained by various simulation techniques, blue marks those, which are obtained by a variety of single crystal experiments. The other results are obtained experimentally on bulk polycrystalline samples. It becomes immediately clear that single crystal experiments always result in much softer higher-order deformation systems than experiments on polycrystalline material, disregarding whether pure Mg or alloys were investigated. For the polycrystalline material a clear (but not dramatic) effect of alloying is visible by a drop of CRSS ratio from around 100 to around 20 to 50 for AZ31 and for Ca-containing alloys. From these observations we conclude that there are two contributions to ductilization: one is related to a moderate change of slip system activation, one is somehow related to the presence or absence of grain boundaries.

The decreasing CRSS ratio for our own Ca-containing alloys may be interpreted either as an increase of the CRSS of basal slip or a decrease of the CRSS of the other de-

Table 5
Compilation of CRSS ratio values obtained in this work and in literature for pure Mg and different alloys. Data marked in yellow are obtained by theoretical simulations. Data marked in blue are obtained from single crystal experiments. All other data are experimental data obtained from polycrystals.

	Materials/Method and reference	B	P0	PI<a>	PI<c+a>	PII<c+a>	Ext Twin
pure Mg	MD simulation [25]	1	22			366 ... 394	
	Sxx and Polycrystal CP-model [26]	1	20-50		40-80		
	CPFEM [38]		14.3		22.3		2
	Polycrystal Experiment [27]	1	48-96				
	Single crystal compression, [28]	1				100	
	Micropillar compression, [29]	1				2	
	microshear, unpublished own group	1			5		
Mg alloys	AZ31/CPFEM [30]	1	18			22	6
	AZ31/ modeling [31]	1	3.2			5	1.5
	AZ31/ VPSC [32]	1	2-8.7		3.4-11.1		1.2-5.2
	AZ31/ FE [32]	1	2-191		3-191		0.7-33
	AZ31/ EPSC, [32]	1	2.8-5.5		3.2-8.3		1.2-5
	Mg-1Mn-0.5Nd/ CPFEM [38]	1	5.4		6.25		2
	Mg-1Mn-1Nd/ CPFEM [38]	1	1.15		1.25		1.05
	Mg-5wt% Y/ 3DXRD observation and S-factor analyses in Extruded [33]	1	1.8-2.7	1.6-1.8			
	Mg 0.4 Y/ Micropillar, [34]	1				4	
	Mg 4 Y/ Micropillar, [34]	1			3		
	Mg-Zn-Nd/ Nanoindentation, [35]	1			13		
	Mg-0.1 at% Al/ Single crystal tension [36]	1	45				
	Mg-0.005 at.% Zn/ Single crystal tension [37]	1	83				
	Mg-0.019 at% Zn (-)		61				
	Mg-0.054 at% Zn (-)		51				
	Mg-0.258 at% Zn (-)		25				
	Mg-0.45 at% Zn(-)	1	16				
Present investigation	X01	1	6	12	24	32	4
	AX101	1	6	12	33	27	4
	AX100	1	7	10	19	52	4
	AZX2101	1	5	8	21	26	5

formation systems. Both mechanisms would finally result in a more balanced activation of the different slip systems, viz. more homogeneous deformation, which, in turn, would reduce the elastic back-stress stresses building up during deformation and lead to more balanced strain hardening. We assume that this is the reason for the observed increase in elongation for the Ca-containing alloys compared to pure magnesium. If the CRSS for basal slip would increase significantly (i.e. by the observed factor of 2), the yield strength would have to increase significantly. This is, however, not the case and we thus assume that, instead, the prismatic and pyramidal systems become softer. Very recently, Zhu et al. [40] and Chaudry et al. [41] demonstrated that the addition of Ca increases the frequency of non-basal $<a>$ slip more than that of $\langle c+a\rangle$ slip. Theses authors attributed the improved tensile elongation to the activation of P_0 and $P_{I<a>}$ slip systems. We think, however, that $\langle a\rangle$ slip alone, even if it is activated together with extension twinning, is not sufficient to guarantee ductile deformation. Extension twinning in Mg is polar in nature and the shear provided by extension twin is only 7%. $\langle a\rangle$ slip and extension twins also do not help to weaken the deformation texture. This is why operation of $\langle c+a\rangle$ slip is essential to achieve considerable ductility [42]. Indeed, we clearly observe activation of $\langle c+a\rangle$ slip on both, the P_I and P_{II} planes from slip trace analyses in all investigated alloys. Refering to the CRSS ratio calculations, the frequency of appearance

of $\langle c+a \rangle$ slip increases with higher Ca content; the AX100 alloy shows less activation of $\langle c+a \rangle$ and an increased P_0 and P_{II} CRSS ratio compared to the alloy AX101. It should be noted that the extension twinning fraction for different alloys obtained from EBSD analyses after 5% elongation is similar for all alloys. Contraction twins and double twins, in contrast, were observed only in AZX2101 alloy. The activation of contraction and double twin has been frequently reported in rare-earth containing Mg alloys. Sandlöbes et al. [1] suggested that the addition of Y in Mg reduces the CRSS for double twin. This conclusion indicates again that the CRSS for the soft deformation systems is not changed, rather that for the harder systems is reduced. Sandlöbes et al. [1] and Barnett [43] suggested that the occurrence of double twins allows c-axis deformation, reduces the uniform elongation and hardening rate and leads to shear localisation at room temperature.

4.5. Grain boundary strength

The results in Fig. 6 show that even though the CRSS ratios for the X01 and AZX2101 alloys are comparable, the latter one exhibits 60% more tensile elongation compared to the former one. Furthermore, the latter alloy exhibits relatively low grain boundary decohesion, thus its improved ductility may be understood to be, at least partly, due to improved grain boundary cohesion strength. Zeng et al. [12] and Bian et al. [44] recently reported that grain boundary cracking affected random high angle boundaries in their Mg-Ca alloys. As all investigated alloys in the present study show largely similar initial microstructures (i.e. grain size and texture) it may be assumed that the grain boundary character should not play any additional role in the present context of grain boundary de-cohesion. Zeng et al. hypothesized chemical segregation to the grain boundaries as possible reason of the grain boundary cracking in their Mg-0.1 at.% Ca, Mg-0.4 at.% Ca and Mg-0.4 at.% Zn alloys. Nevertheless, these authors did not present measurements for their hypothesis. Here we employed for the first time atom probe tomography to investigate the particular roles of Ca and Zn on the grain boundary chemistry and its possible embrittlement. As presented in section 3.3, Ca segregates in form of clusters in alloy X01. The Ca-content in these clusters is an order of magnitude higher than the average GB composition in the selected alloys. Grain boundary segregation in Mg alloys with rare earth elements, e.g. Y or Gd was earlier reported by [45,46]. Bugnet et al. reported the formation of “fcc Gd clusters” during the homogenization treatment of a Mg-0.3 at.% Gd alloy. Periodic segregation patterns of Gd and Zn in coherent twin boundaries was reported by Nie et al. [47]. These author claimed that positive and negative atomic size-misfit of Gd and Zn leads to segregation on the expanded and contracted sites along the twin boundaries. Huber et al. [48] further showed by using DFT that the rare-earth elements and Ca increase the binding energy in $\Sigma 7$ boundaries. Co-segregation of Zn and Ca was earlier observed using HRTEM by Zeng et al. [49]. These authors also anticipated that positive and negative size misfit of segregating atoms with a size between that of Ca and Zn relative to Mg help co-segregation at expansion and contraction zones of a grain boundary dislocation core, respectively. The authors also suggested that co-segregation of Ca and Zn makes grain boundaries less mobile compared to only Ca or only Zn segregation. In this present study we realized that co-segregation of Zn and Ca in AZX2101 helps to improve the grain boundary strength unlike only Ca segregation in X01 alloy. Using ab-initio simulations, Hase et al. [50] also indicated improved grain boundary cohesion strength in Mg alloys with adding Ca and Zn or Al.. Kula et al. [51,52] also argued that segregation of Gd and Y atoms at grain boundaries in Mg–Gd and Mg–Y alloys may improve the grain boundary cohesion strength. In our case, the results in Figs. 8 and 9 clearly indicate improved grain boundary cohesion strength in alloy AZX2101 compared to alloy X01. Further, inference can be made from the tensile fracture surfaces: the alloy AZX2101 exhibits more dimple like features (Fig. 3(d)) whereas X01 mostly shows fracture along grain boundaries (Fig. 3(a)). Therefore, even though Ca in Mg increases the intrinsic activity of non-basal slip in X01 alloy its elongation is limited due to grain boundary cracking. According to equilibrium calculations, addition of Zn and/or Al prevent the formation of Mg_2Ca Laves phase. This could indicate that the tendency of Ca atoms to cluster at grain boundaries is reduced by addition of Zn as well.

Sun et al. [53] studied the role of intergranular deformation in an extruded Mg–8Gd–3Y alloy. They discussed that the immense activation of basal slip generates severe grain boundary incompatibility and rises the incompatibility stress. They pointed out that this extra strain incompatibility at the grain boundary can be accommodated if grain boundary connectivity favours dislocation transfer across the boundary. On the other hand, Shi et al. [23] demonstrated that Al and Zn additions reduce the connectivity of grains that are orientated for basal slip. So, it can be surmised that the addition of Al and Zn resists slip transfer and thus builds up strain incompatibility. Activation of non-basal slip systems and contraction and/or double twins is, in general, difficult and requires high resolved shear stresses. Therefore, these deformation systems will be activated only when the grain boundary can withstand such high and localized stresses built-up at the boundaries. Both, non-basal slip systems and contraction and double twins are activated in the 5% deformed AZX2101 alloy which supports the assumption of increased grain boundary strength in this alloy compared to that of any other Mg alloy. Koike et al. [42] earlier speculated that activation of basal slip leads to a rise of the grain boundary compatibility stresses. Only when the grain boundary is strong enough non-basal slip and contraction and double twin systems get activated [54]. Fig. 9(b) shows that once the tensile curve is modified by the true cross section, reduced by the cracked grain boundary area, the mechanical flow curves of alloys X01 and AZX2101 are almost coinciding. This observation indicates that grain boundary cracking acts as a “weakening” mechanism which limits the otherwise beneficial effect that Ca-additions equalize the CRSS ratios in these alloys. The addition of Zn thus improves the hardening capacity in the

alloy AZX2101 by preventing grain boundary cracking and consequently increases the ductility.

To summarize, Al addition increases the strength of the alloy by solid solution strengthening of ⟨a⟩ slip. Ca addition balances the CRSS ratios for non-basal slip systems, however, the 'exploitable' ductility associated with this beneficial effect is limited due to inherently weak grain boundaries. Finally, addition of Zn changes the character of Ca segregation at the GB, resulting in improved grain boundary strength which withstand the incompatibility stress at the boundaries. Consequently, it improves the materials's ductility further. Hitherto, it is clear that in addition to the activation of pyramidal non-basal slip systems, tailoring the nature of grain boundary segregation to improve grain boundary cohesion is crucial in designing formable and strong non-RE Mg alloys for instance for advanced sheet forming applications.

5. Conclusions

The present study comprehensively demonstrates the intrinsic effect of Ca, Zn and Al on the room temperature tensile elongation of Mg alloys. From the obtained results and the above discussion, we draw the following conclusions:

1. The addition of a small amount of Ca to Mg alloys improves the ductility. This is due to a decrease of the critical resolved shear stresses of higher-order deformation systems relative to that for basal slip by a factor of 2 to 4. This, altogether leads to a more balanced activation of slip systems. It is assumed that the higher order deformation systems become softer, rather than basal slip becoming harder, which explains the general weakening effect of Ca additions. We do not attempt to explain the mechanisms by which Ca softens the higher order deformation systems.
2. Ca has a tendency to form Ca-rich clusters on grain boundaries in Mg which reduce the grain boundary strength. The clusters form even when Ca is present as a dilute addition up to 0.1 wt% (=0.06 at-%). We believe that they are a precursor of Laves phase Mg_2Ca which forms if the Ca content of the alloy becomes too high (> 0.1 at-%).
3. The addition of Zn mainly improves grain boundary strength by increasing the grain boundary cohesion and reducing the formation of the above-mentioned Ca-rich clusters on the boundaries in Ca-containing alloys. In this way, Zn plays a major role in improving both, strength and ductility of Mg-alloys: the increased strength of the boundaries allows the applied stresses to reach values high enough to activate the necessary higher-order deformation systems without grain boundary cracking.
4. The addition of Al alone generally strengthens Mg alloys but does not significantly improve their ductility.
5. The addition of Ca, Al and Zn in appropriate amounts and ratios to Mg thus leads to a non-RE containing alloy class with high ductility and high strength due to the beneficial interaction of all mechanisms mentioned under points 1 to 4.

Acknowledgement

One of the authors (SN) acknowledges the financial support by the international doctoral school IMPRS, Surmat. SN also acknowledges valuable discussion with Prof. S. Sandlöbes and Prof. G. Dehm.

Supplementary material

Supplementary material associated with this article can be found, in the online version, at doi:10.1016/j.jma.2021.03.005.

References

[1] S. Sandlöbes, S. Zaefferer, I. Schestakow, S. Yi, R. Gonzalez-Martinez, Acta Mater. (2011), doi:10.1016/j.actamat.2010.08.031.
[2] S. Sandlöbes, Z. Pei, M. Friák, L.F. Zhu, F. Wang, S. Zaefferer, D. Raabe, J. Neugebauer, Acta Mater. 70 (2014) 92–104, doi:10.1016/j.actamat.2014.02.011.
[3] M.H. Yoo, S.R. Agnew, J.R. Morris, K.M. Ho, Mater. Sci. Eng. A (2001), doi:10.1016/S0921-5093(01)01027-9.
[4] P.J.F. Stohr, J.P. Poirier, Philos. Mag. 25 (1972) 1313–1329, doi:10.1080/14786437208223856.
[5] J. Geng, M.F. Chisholm, R.K. Mishra, K.S. Kumar, Philos. Mag. Lett. 94 (2014) 377–386, doi:10.1080/09500839.2014.916423.
[6] Z. Wu, W.A. Curtin, Nature 526 (2015) 62–67, doi:10.1038/nature15364.
[7] Z. Wu, R. Ahmad, B. Yin, S. Sandlöbes, W.A. Curtin, Science 359 (2018) 447–452 80-.
[8] M.H. Yoo, J.R. Morris, K.M. Ho, S.R. Agnew, Metall. Mater. Trans. A Phys. Metall. Mater. Sci. 33 (2002) 813–822, doi:10.1007/s11661-002-1013-5.
[9] Y. Tang, J.A El-Awady, Acta Mater. 71 (2014) 319–332, doi:10.1016/j.actamat.2014.03.022.
[10] Y. Chino, T. Ueda, Y. Otomatsu, K. Sassa, X. Huang, K. Suzuki, M. Mabuchi, Mater. Trans. 52 (2011) 1477–1482, doi:10.2320/matertrans.M2011048.
[11] S. Sandlöbes, M. Friák, S. Korte-Kerzel, Z. Pei, J. Neugebauer, D. Raabe, Sci. Rep. 7 (2017) 1–8, doi:10.1038/s41598-017-10384-0.
[12] Z.R. Zeng, M.Z. Bian, S.W. Xu, C.H.J. Davies, N. Birbilis, J.F. Nie, Mater. Sci. Eng. A 674 (2016) 459–471, doi:10.1016/j.msea.2016.07.049.
[13] J.A. del Valle, F. Carreño, O.A. Ruano, Acta Mater. (2006), doi:10.1016/j.actamat.2006.05.018.
[14] J. Hirsch, T. Al-Samman, Acta Mater. 61 (2013), doi:10.1016/j.actamat.2012.10.044.
[15] H. Li, D.E. Mason, T.R. Bieler, C.J. Boehlert, M.A. Crimp, Acta Mater. 61 (2013) 7555–7567, doi:10.1016/j.actamat.2013.08.042.
[16] Z. Wang, S. Zaefferer, Mater. Charact. 130 (2017) 33–38, doi:10.1016/j.matchar.2017.05.023.
[17] A.J. Wilkinson, G. Meaden, D.J. Dingley, Ultramicroscopy 106 (2006) 307–313, doi:10.1016/j.ultramic.2005.10.001.
[18] A. Tripathi, S. Zaefferer, Ultramicroscopy 207 (2019) 112828, doi:10.1016/j.ultramic.2019.112828.
[19] H. Shou, J. Zheng, Y. Zhang, D. Long, J. Rao, Q. Liu, J. Alloys Compd. 784 (2019) 1187–1197, doi:10.1016/j.jallcom.2019.01.159.
[20] R. Pei, S. Korte-Kerzel, T. Al-Samman, Mater. Sci. Eng. A 763 (2019) 138112, doi:10.1016/j.msea.2019.138112.
[21] X. Huang, K. Suzuki, M. Yuasa, Y. Chino, Mater. Sci. Eng. A 587 (2013) 150–160, doi:10.1016/j.msea.2013.08.067.

[22] K.H. Kim, J.H. Hwang, H.S. Jang, J.B. Jeon, N.J. Kim, B.J. Lee, Mater. Sci. Eng. A (2018), doi:10.1016/j.msea.2018.01.010.
[23] D.F. Shi, Acta Mater. (2019), doi:10.1016/j.actamat.2019.09.018.
[24] Y. Chino, T. Ueda, M. Kado, M. Mabuchi, Mater. Trans. 52 (2011) 1840–1843, doi:10.2320/matertrans.M2011109.
[25] K.H. Kim, J.B. Jeon, N.J. Kim, B.J. Lee, Scr. Mater. 108 (2015) 104–108, doi:10.1016/j.scriptamat.2015.06.028.
[26] S. Graff, W. Brocks, D. Steglich, Int. J. Plast. 23 (2007) 1957–1978, doi:10.1016/j.ijplas.2007.07.009.
[27] W.B. Hutchinson, M.R. Barnett, Scr. Mater. 63 (2010) 737–740, doi:10.1016/j.scriptamat.2010.05.047.
[28] T. Obara, H. Yoshinga, S. Morozumi, Acta Metall. 21 (1973) 845–853, doi:10.1016/0001-6160(73)90141-7.
[29] E. Lilleodden, Scr. Mater. 62 (2010) 532–535, doi:10.1016/j.scriptamat.2009.12.048.
[30] A. Chapuis, Q. Liu, J. Magnes. Alloy 7 (2019) 433–443, doi:10.1016/j.jma.2019.04.004.
[31] A. Jain, S.R. Agnew, Mater. Sci. Eng. A 462 (2007) 29–36, doi:10.1016/j.msea.2006.03.160.
[32] B. Raeisinia, S.R. Agnew, A. Akhtar, Metall. Mater. Trans. A Phys. Metall. Mater. Sci. 42 (2011) 1418–1430, doi:10.1007/s11661-010-0527-5.
[33] Z. Huang, L. Wang, B. Zhou, T. Fischer, S. Yi, X. Zeng, Scr. Mater. 143 (2018) 44–48, doi:10.1016/j.scriptamat.2017.09.011.
[34] J. Wu, S. Si, K. Takagi, T. Li, Y. Mine, K. Takashima, Y.L. Chiu, Philos. Mag. 100 (2020) 1454–1475, doi:10.1080/14786435.2020.1725250.
[35] G. Nayyeri, W.J. Poole, C.W. Sinclair, S. Zaefferer, Scr. Mater. 156 (2018) 37–41, doi:10.1016/j.scriptamat.2018.07.003.
[36] A. Akhtar, E. Teghtsoonian, Philos. Mag. 25 (1972) 897–916, doi:10.1080/14786437208229311.
[37] A. Akhtar, E. Teghtsoonian, Acta Metall. 17 (1969) 1351–1356.
[38] V. Herrera-Solaz, P. Hidalgo-Manrique, M.T. Pérez-Prado, D. Letzig, J. Llorca, J. Segurado, Mater. Lett. 128 (2014) 199–203, doi:10.1016/j.matlet.2014.04.144.
[39] N. Stanford, M.R. Barnett, Int. J. Plast. (2013), doi:10.1016/j.ijplas.2013.01.012.
[40] G. Zhu, L. Wang, H. Zhou, J. Wang, Y. Shen, P. Tu, H. Zhu, W. Liu, P. Jin, X. Zeng, Int. J. Plast. 120 (2019) 164–179, doi:10.1016/j.ijplas.2019.04.020.
[41] U.M. Chaudry, T.H. Kim, S.D. Park, Y.S. Kim, K. Hamad, J.G. Kim, Mater. Sci. Eng. A 739 (2019) 289–294, doi:10.1016/j.msea.2018.10.060.
[42] J. Koike, T. Kobayashi, T. Mukai, H. Watanabe, M. Suzuki, K. Maruyama, K. Higashi, Acta Mater. (2003), doi:10.1016/S1359-6454(03)00005-3.
[43] M.R. Barnett, Mater. Sci. Eng. A 464 (2007) 8–16, doi:10.1016/j.msea.2007.02.109.
[44] M.Z. Bian, Z.R. Zeng, S.W. Xu, S.M. Zhu, Y.M. Zhu, C.H.J. Davies, N. Birbilis, J.F. Nie, Adv. Eng. Mater. 18 (2016) 1763–1769, doi:10.1002/adem.201600293.
[45] M. Bugnet, A. Kula, M. Niewczas, G.A. Botton, Acta Mater. 79 (2014), doi:10.1016/j.actamat.2014.06.004.
[46] J.P. Hadorn, T.T. Sasaki, T. Nakata, T. Ohkubo, S. Kamado, K. Hono, Scr. Mater. 93 (2014), doi:10.1016/j.scriptamat.2014.08.022.
[47] J.F. Nie, Y.M. Zhu, J.Z. Liu, X.Y. Fang, Science 340 (2013) 957–960 80-, doi:10.1126/science.1229369.
[48] L. Huber, J. Rottler, M. Militzer, Acta Mater. 80 (2014) 194–204, doi:10.1016/j.actamat.2014.07.047.
[49] Z.R. Zeng, Y.M. Zhu, S.W. Xu, M.Z. Bian, C.H.J. Davies, N. Birbilis, J.F. Nie, Acta Mater. 105 (2016), doi:10.1016/j.actamat.2015.12.045.
[50] T. Hase, T. Ohtagaki, M. Yamaguchi, N. Ikeo, T. Mukai, Acta Mater. 104 (2016) 283–294, doi:10.1016/j.actamat.2015.11.045.
[51] A. Kula, X. Jia, R.K. Mishra, M. Niewczas, Int. J. Plast. 92 (2017) 96–121, doi:10.1016/j.ijplas.2017.01.012.
[52] A. Kula, K. Noble, R.K. Mishra, M. Niewczas, Philos. Mag. 96 (2016) 134–165, doi:10.1080/14786435.2015.1123820.
[53] J. Sun, L. Jin, J. Dong, F. Wang, S. Dong, W. Ding, A.A. Luo, Int. J. Plast. 123 (2019) 121–132, doi:10.1016/j.ijplas.2019.07.014.
[54] J. Koike, Metall. Mater. Trans. A Phys. Metall. Mater. Sci. 36 (2005) 1689–1696, doi:10.1007/s11661-005-0032-4.